Composition-adjustable silicon-germanium alloy films based on porous silicon matrices

Nikita Grevtsov [a],[*], Eugene Chubenko [a], Vitaly Bondarenko [a], Ilya Gavrilin [b], Alexey Dronov [b], Sergey Gavrilov [b], Grigory Rymski [c], Kazimir Yanushkevich [c], Dmitry Goroshko [d], Efim Argunov [e]

[a] *Belarusian State University of Informatics and Radioelectronics, Minsk, Belarus*
[b] *National Research University of Electronic Technology, Zelenograd, Moscow, Russia*
[c] *Scientific-Practical Materials Research Centre of NAS of Belarus, Minsk, Belarus*
[d] *Institute of Automation and Control Processes of FEB RAS, Vladivostok, Russia*
[e] *National University of Science and Technology MISiS, Moscow, Russia*

ARTICLE INFO

ABSTRACT

Morphology and crystalline structure of silicon-germanium alloys formed by rapid thermal processing of germanium-filled porous silicon layers are evaluated. Two types of porous silicon are employed as matrices for electrochemical pore filling using GeO_2 aqueous solutions and subsequently compared, the first one formed by electrochemical anodization and the second by silver-assisted chemical etching of monocrystalline silicon. The resulting alloys' structure and composition are investigated using scanning electron microscopy, energy-dispersive X-ray analysis, Raman spectroscopy and X-ray powder diffraction. It is shown that by varying the porosity of the initial matrix (by adjusting anodization current density for anodic porous silicon or changing silver deposition time for structures produced by metal-assisted etching) in the range from 55 to 75%, $Si_{1-x}Ge_x$ alloys with germanium fractions of $x = 0.31$ to $x = 0.83$ can be formed, as indicated by Raman spectroscopy. It is concluded that composition-adjustable layers of silicon-germanium can be successfully formed on either type of porous silicon layer. While an increase in porosity generally leads to a decrease in silicon fractions in the alloy, the steepness of this effect varies heavily depending on the type of porous matrix used and should be considered independently for anodic porous silicon and silicon nanowires.

1. Introduction

Silicon-germanium alloys ($Si_{1-x}Ge_x$) are mostly prominent for their application in efficient high-temperature thermoelectric devices utilized in extreme conditions, such as thermoelectric generators converting radioisotope heat into electricity for deep space missions [1]. Research on thermoelectric materials took a new turn in the 1990 s along with rapid development of nanotechnology, which opened up new prospects for improving device efficiency [2]. In addition to conventional bulk methods such as zone melting and powder metallurgy, various approaches to nanostructuring and formation of thin films emerged, each providing their own sets of benefits. Compared to traditional bulk methods, thin film techniques generally do not allow the same degree of control over alloy composition. However, they offer unique advantages, as the resulting films can be easily integrated into small-scale devices and are more suitable for applications requiring the coverage of large

surface areas, also meaning that a larger temperature gradient can be established [3].

Vapor deposition techniques (physical — PVD, and chemical — CVD) continue to be among the most popular approaches to $Si_{1-x}Ge_x$ film fabrication and are usually carried out using SiH_4 (silicon precursor), GeH_4 (germanium precursor), H_2 and HCl gas mixtures. The low-pressure chemical vapor deposition (LPCVD) method remains the most widely used approach due to its reproducibility, homogeneity and higher throughput, with a drawback of low deposition rate [4].

Another widespread method is molecular beam epitaxy (MBE) wherein materials are grown under ultrahigh vacuum conditions on a preheated monocrystalline substrate using substance evaporated from a molecular source. The resulting layers possess an identical or similar crystalline structure to the substrate, leading to no more than 10% lattice mismatch between the film and the surface. Some of the other likely advantages of MBE over CVD include lower operating temperatures,

greater precision in controlling film composition and thickness, and the ability to fabricate complex Si-based structures and superlattices. Disadvantages inherent to MBE are the relatively low growth rates, as well as contamination due to chemisorbed oxygen or carbon from the substrate or residual gas exposure [5]. Liquid-phase epitaxy (LPE or liquid melt growth) is based on growing a crystalline alloy layer from a solution or precursor melt. The silicon-germanium alloy crystallizes on the surface of a substrate which is immersed in the precursor as it cools. LPE's higher growth rate enables acquisition of dense $Si_{1-x}Ge_x$ layers with different compositions and thicknesses up to 20 μm. The resulting layers are characterized by lower dislocation densities compared to materials obtained by MBE and CVD due to growth near equilibrium. However, higher lattice mismatch and poor thickness control are reported [6], and the technique itself requires maintaining high vacuum conditions inside the growth chamber.

Magnetron sputtering followed by annealing offers yet another failsafe, relatively inexpensive, and environmentally friendly method of producing silicon-germanium films, including those on insulating substrates. $Si_{1-x}Ge_x$ films deposited by this method are initially amorphous and crystallize under various annealing conditions. Bulk germanium samples mounted on a silicon wafer can be used as sputtering targets; in this case, the germanium fraction in the resulting alloy can be controlled by adjusting the ratio of surface areas of Ge and Si exposed to argon plasma [7].

Recently, the so-called layer exchange method has also been introduced, which involves the exchange of alternating metal and semiconductor films as a result of their thermal processing. To conduct this process, a metal layer and an amorphous semiconductor layer (5 to 500 nm) are sequentially deposited onto an arbitrary substrate and subsequently heat-treated in inert gas atmosphere at a temperature below the eutectic point. During this annealing step, the atoms of the semiconductor material diffuse from the amorphous layer into the metal layer. When their concentration in the metal exceeds the saturation limit, semiconductor nucleation occurs. Semiconductor atoms, being dissolved in the metal, come into contact with the nuclei, causing lateral growth of semiconductor crystals. This in turn leads to mechanical stresses and pushes the metal upward. Eventually, the crystalline semiconductor forms the bottom layer, while the metal forms the top layer. Thermodynamically, the driving force of this process is the difference in Gibbs free energy between the amorphous and crystalline semiconductor. The metastability and high free energy of the amorphous layer causes oversaturation, which leads to nucleation in the metal layer. Therefore, the initial semiconductor layer must be amorphous or at least weakly crystalline to carry out the exchange process. As such, the process itself is irreversible [8].

Despite recent advances, the respective approaches remain relatively underdeveloped due to the difficulties in fabrication and characterization of $Si_{1-x}Ge_x$ films. Additionally, they all are characterized by the need for complex equipment and/or expensive precursor materials, greatly complicating their practical implementation. As such, the development of a simpler approach remains an important task.

In 1956 Arthur Uhlir (Bell Labs, Murray Hill, New Jersey) established the possibility of forming porous silicon (PS) — a new structural and morphological form of silicon [9]. Since then, many approaches (mostly chemical and electrochemical in nature) to fabricating diverse forms of PS have been established and documented, enabling researchers to synthesize a large selection of porous morphologies suitable for a variety of practical tasks [10–14]. PS's broad range of applications stems from its highly developed structure, letting it possess a characteristic set of physical and chemical properties not akin to its monocrystalline counterpart, most of which can be easily adjusted by altering the processing parameters. One of the most promising applications of PS is its use as a porous matrix for subsequent filling with other materials. The resulting composites can exhibit characteristics inherent neither to the matrix nor to the guest material, all the while being fully compatible with most of the currently employed semiconductor manufacturing processes. The

list of suitable guest materials includes but is not limited to metals and semiconductors [15], with the latter posing an especially large practical interest in the context of the present work.

As we have previously established, either of the two basic vertical forms of PS (anodic PS formed by electrochemical anodization and vertically-aligned arrays of silicon nanowires (SiNWs) formed by metal-assisted chemical etching (MACE)) can be successfully used as matrices and filled with germanium, demonstrating satisfactory reproducibility and pore filling factors. Electrochemical liquid-liquid solid growth (ec-LLS) was first employed to obtain germanium deposits, requiring preliminarily deposited fusible metal particles to act as nucleation points and electron suppliers for rapid semiconductor growth [16]. However, while utilizing ec-LLS with indium particles serving as precursors was originally suspected to be the only way to achieve reproducible pore filling, a successful way of obtaining germanium deposits without any preliminary fusible metal coverage was later discovered [17]. Furthermore, by subjecting either type of PS filled with germanium to heat treatment, a $Si_{1-x}Ge_x$ layer can be reproducibly formed, provided that certain processing conditions are met [18]. Presumably, if thoroughly studied and successfully adopted as a technological process, this approach to the formation of silicon-germanium can prove to be significantly more cost-effective compared to the currently employed alternatives [19]. As opposed to the above-listed approaches to $Si_{1-x}Ge_x$ film synthesis, thermal treatment of PS filled with germanium is expected to be more cost-effective due to a combination of availability and cheapness of all the necessary materials, relatively high level of control over alloy composition, no need for complex equipment, and possibility of direct integration with technological processes of the semiconductor industry.

The present work's primary objective is performing a complex study of $Si_{1-x}Ge_x$ layers capable of being produced via thermal processing of silicon-germanium composites obtained by depositing germanium into anodic PS and SiNW arrays. Presumably, by controlling the initial porous layer's structural parameters, the quantitative ratio of elements in the resulting alloy can be directly controlled, enabling reproducible acquisition of any required subtype of alloy.

2. Materials and methods

2.1. Processing

All chemical and electrochemical processing stages listed below were carried out in a PTFE electrochemical cell, with contact to the back of the working electrode (silicon sample) implemented by pressing the latter down to an underlying graphite disk. A platinum wire served as a counter-electrode for electrochemical processing, and the according regimes were set using a Metrohm Autolab PGSTAT302N potentiostat/galvanostat.

Anodic PS layers were formed on highly (0.01 Ohm·cm) antimony-doped monocrystalline (100)-oriented n-type silicon wafers by means of their electrochemical anodization using a solution containing hydrofluoric acid, deionized water and isopropyl alcohol mixed in a volume ratio of 1:3:1. Current densities of 50, 70 and 90 mA/cm^2 were used to form PS layers with varying porosities and structural parameters. The anodization time was adjusted for each current density to obtain layers of comparable thickness (roughly 1.5 μm). Due to PS's formation mechanism, its subsurface layer (about 0.3 μm from its topmost edge) exhibits smaller pore sizes, which, as it was established in a series of preliminary experiments, significantly complicates pore filling and does not allow to draw any conclusions regarding the structure of underlying layers on the basis of surface SEM images [20]. As such, the layer in question was preliminarily removed using a two-stage procedure. The first stage involved chemical deposition of copper [21] performed by immersing PS in an aqueous solution containing 0.03 M $CuSO_4$ and 0.14 M HF for 3 min, leading to complete localization of copper in the subsurface layer. At the second stage, the copper was etched in 20% HNO_3

for 5 min, simultaneously resulting in subsurface layer removal. Since nitric acid treatment leads to silicon's oxidation, each anodic PS sample was additionally immersed in 4.5% hydrofluoric acid to remove the oxide layer. This process was carried out for a relatively long period of time (1 h) to take into account capillary effects that slow the access of HF into the pore channels. The resulting PS layer with its subsurface layer removed will be referred to simply as "PS" or "anodic PS".

Arrays of SiNWs were produced on lightly (12 Ohm·cm) boron-doped monocrystalline (100)-oriented p-type silicon wafers by MACE using silver particles. The latter were preliminarily deposited onto each sample's surface by immersing it in a water solution containing 0.01 M AgNO$_3$, 2.64 M HF and 1.28 M C$_2$H$_5$OH for 15, 30 or 60 s, with the time period in question directly dictating the porosity value. Etching was subsequently conducted using an aqueous solution containing 4.37 M HF and 0.279 M H$_2$O$_2$ (with the latter serving as an oxidant) for 8 min, yielding porous layers approximately 2 μm in thickness. Indium was then deposited into the resulting SiNWs using a water solution containing 0.019 M In$_2$(SO$_4$)$_3$ at a current density of 0.5 mA/cm^2 for 10 min. Since the silver particles previously used as a mask remain in the SiNWs' bottommost parts, they serve as favorable nucleation points for indium particles, completely localizing the fusible metal inside the pores. While pulsed electrodeposition was previously employed in order to avoid subsurface indium nucleation [16], it was later found that simply reducing indium's concentration enables similarly favorable results.

Germanium deposition was carried out on preemptively air-dried samples using a solution containing 0.05 M GeO$_2$, 0.5 M K$_2$SO$_4$ and 0.1 M C$_4$H$_6$O$_4$ (succinic acid) with pH adjusted to 6.5 using NH$_4$OH. The solution's temperature was maintained at an 85 °C mark under magnetic stirring. In the case of anodic PS, the deposition process was carried out for 30 min at a current density of 2 mA/cm^2, while a 15 min deposition process at 6 mA/cm^2 was employed for MACE-produced samples due to the difference in germanium's nucleation and growth mechanisms. To obtain a Si$_{1-x}$Ge$_x$ layer, germanium-filled PS of either type was subjected to rapid thermal processing (RTP) using an Annealsys As-One 100 RTP system. Annealing was conducted at 950 °C over the course of 30 s under argon flow (800 sccm). This temperature value lies above germanium's melting point, leading to the latter's alloying with PS's sidewalls. Naturally, the alloyed film's thickness is expected to be equal to or lower than that of the initial porous layer.

2.2. Analysis

The samples' crystal structure and phase composition were evaluated using a DRON-3 X-ray diffractometer (XRD) in CuKα radiation (λ = 0.15406 nm) at room temperature, with an exposure time of 4 s and a step of 0.02°. XRD pattern matching was performed using *PCPDF-WIN* and *Jana2006* software, as well as *The Materials Project* database. The layer's morphology and elemental composition were studied with a Hitachi S-4800 scanning electron microscope (SEM) equipped with a Bruker QUANTAX 200 spectrometer for energy dispersive X-ray spectroscopy (EDX) measurements. For distribution comparison, element concentration profiles were obtained by scanning each sample diagonally across the porous layer. It should be noted that this particular method of elemental analysis relies on acquiring the X-ray spectra from a volume of around 0.5 μm^3. Since the structures in question generally fall below this size threshold, the data obtained via this method (EDX concentration profiles and maps) can be perceived as average throughout said volume and are therefore expressed in arbitrary units (a.u.). As the conditions of the EDX analysis remained unchanged for all the samples discussed in the present work, we consider this approach reasonable due to only using these concentration values as means of spatial distribution comparison [16]. A Confotec NR500 3D scanning laser confocal Raman microscope equipped with a 473 nm 25 mW Cobolt Blues blue laser was used to analyze the surface composition and quantify the amount of germanium and silicon-germanium present in each case. Since EDX provides solely quantitative data, and we expect significant fractions of

the materials to be unalloyed, Raman spectroscopy was the preferred method of stoichiometry analysis. The laser in question had focus beam size of 2.5 μm and a penetration depth of around 0.7 μm in bulk silicon, enabling surface and subsurface characterization. The doping type of each sample has been assessed with the use of the hot-point probe method. The study of electrical conductivity and Seebeck coefficient of the produced SiGe alloy films were carried using a Cryotel system in the temperature range of 300–900 K. To ensure stable contact of measuring probes to the high resistivity sample, aluminum contact pads 1 mm in dimeter were preliminarily deposited onto each sample's surface.

The pores' geometrical parameters were evaluated on the basis of surface SEM imagery using *ImageJ* software. The software's built-in functions enable determination of the pores' average spatial density, area S and equivalent diameter D (as calculated as $D = 2(S/\pi)^{1/2}$ under an assumption that each pore has a circular shape). Additionally, in order to assess the sidewall thickness, an *ImageJ* extension created by Haeri M. et al. [22] was used, wherein the distance T between two pores with equivalent radii of r_1 and r_2 located at x_1, y_1 and x_2, y_2 is calculated as

$$T = \sqrt{(y_2 - y_1)^2 + (x_2 - x_1)^2} - (r_1 + r_2),\qquad(1)$$

Due to the use of equivalent radii, (1) gives the most accurate results when the pores' shapes are closest to circular.

3. Results and discussion

3.1. Anodic porous silicon

Figs. 1–4 show surface, cross-section and bird's-eye-view SEM images, as well as EDX-mapped cross-section SEM images, XRD spectra and Raman spectra of three sample groups presented in accordance with their fabrication order: initial PS samples, samples filled with germanium and the same samples subjected to RTP. The three groups differed in current density used for PS fabrication. As anodization current density is known to directly impact the lateral sizes of pores otherwise prepared under the same processing conditions [11], its value directly determined each layer's porosity. The anodization time was slightly adjusted to accommodate for the difference in etching speed and produce layers of comparable thickness.

A 35 s anodization process at 50 mA/cm^2 yields a layer riddled with vertical pores ranging from 10 to 40 nm in diameter with a placement density of 1.01•10^{11} cm^{-2} and noticeably varying in shades of grey, while the pores in the exposed underlayer range from 30 to 80 nm, possess a significantly reduced density of 2.38•10^{10} cm^{-2} and are identical in color. The pore sidewall thickness remains nearly unchanged regardless of the depth, staying in the range of 7 to 22 nm. Presumably, the darker pores correspond to those seen on the image obtained after subsurface layer removal, which is further reinforced by their similarity in density (1.37•10^{10} cm^{-2}), as well as the black pores' larger sizes. This noticeable difference in layer morphology significantly obstructs ion exchange during electrodeposition, thus the need for an additional removal procedure.

Resulting from anodization at 70 mA/cm^2 for 30 s are vertically-aligned pores ranging in diameter from 20 to 60 nm with a placement density of 9.08•10^{10} cm^{-2} (or 40–100 nm and 1.49•10^{10} after subsurface layer removal) separated by sidewalls up to 30 nm thick.

Lastly, anodizing the wafer at 90 mA/cm^2 for 25 s results in pores exhibiting yet larger equivalent diameters which range from 20 to 65 nm (3.04•10^{10} cm^{-2}) and are increased to the range of 45 to 150 nm (9.60•10^9 cm^{-2}) after subsurface layer removal. Subsequently to the latter, the pore morphology is by far the most defect-free of all samples, yielding trapezoid-shaped pores with clearly distinguished smooth sidewalls. The pore sidewall thickness ranges from 9 to 29 nm.

Regardless of pore size, germanium's electrodeposition occurs throughout the porous layer due to the presence of numerous surface
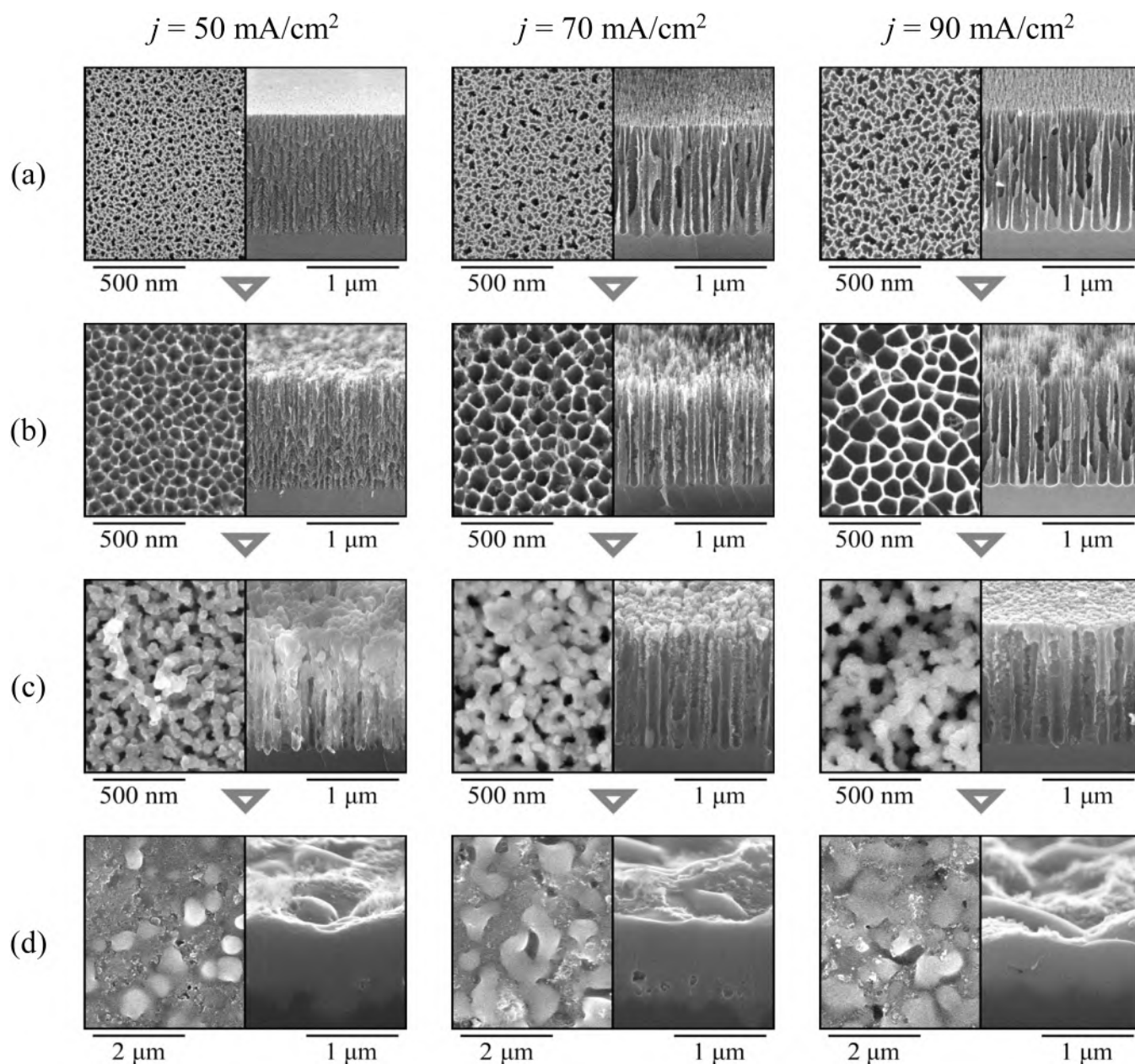
Fig. 1. Surface and bird's-eye view SEM images of samples prepared on the basis of anodic PS with varying anodization current densities *j*: (a) initial PS layer, (b) PS layer with its subsurface layer chemically removed, (c) PS filled with germanium and (d) the resulting samples subjected to RTP.

defects and other potential nucleation points (Fig. 1, c). While the cross-section SEM results demonstrate adequate pore filling, small gaps between germanium-covered sidewalls are still present, as indicated by dark pores up to 60 nm in diameter visible on the surface images.

After being subjected to RTP, dense alloyed layers are formed (Fig. 1, d), with their thicknesses noticeably smaller (0.6–0.9 μm) than those of the initial porous layers due to the aforementioned gaps. Additional cross-section images of the same samples along with the corresponding EDX mapping data are presented in Fig. 2. The latter show that a uniform $Si_{1-x}Ge_x$ layer is formed in the case of either of the three anodization current densities. Noticeably, germanium's concentration is somewhat lacking on the surface, and also starts to decline towards the bottommost half of the layer, which might be caused by the gradual increase in signal accumulation from underlying bulk silicon. This indicates some lateral deviations in alloy composition caused by differences in pore filling.

XRD spectra compiled in Fig. 3 are presented in the 2θ range of 20° to 64°, as the only peak visible beyond that range is the one correlating to

monocrystalline silicon (400) at 2θ = 70°. Notably, the latter is the only peak present when performing XRD analysis of a monocrystalline (100) wafer without a porous layer or any other coverage, and in the case of PS its intensity exceeds those of any other peaks by up to 3 orders of magnitude. The peak at 33.0° is observed on all PS-based samples and can be attributed to either the PS layer or the underlying silicon wafer, pertaining to the (200) orientation (forbidden reflection in Si (100) becoming visible due to multiple diffraction following the well-defined in-plane sample orientation [23,24]). Subsequently to germanium deposition, the peaks characteristic of the guest material are present at 27.2° (Ge (111)), 45.3° (Ge (200)) and 53.7° (Ge (131)) [25]. Lastly, after RTP, additional peaks appear at 27.3° (SiGe (100)), 27.8° (SiGe (111)) and 29.3° (Ge (102)), while the Ge (131) peak increases in intensity, indicating successful silicon-germanium alloying and changes in germanium's crystallinity [26,27]. A silicon dioxide SiO_2 peak is also present at 22.4°, exhibiting a distinctive wide shape due to its amorphous nature [28,29]. Notably, the peak in question is only present after
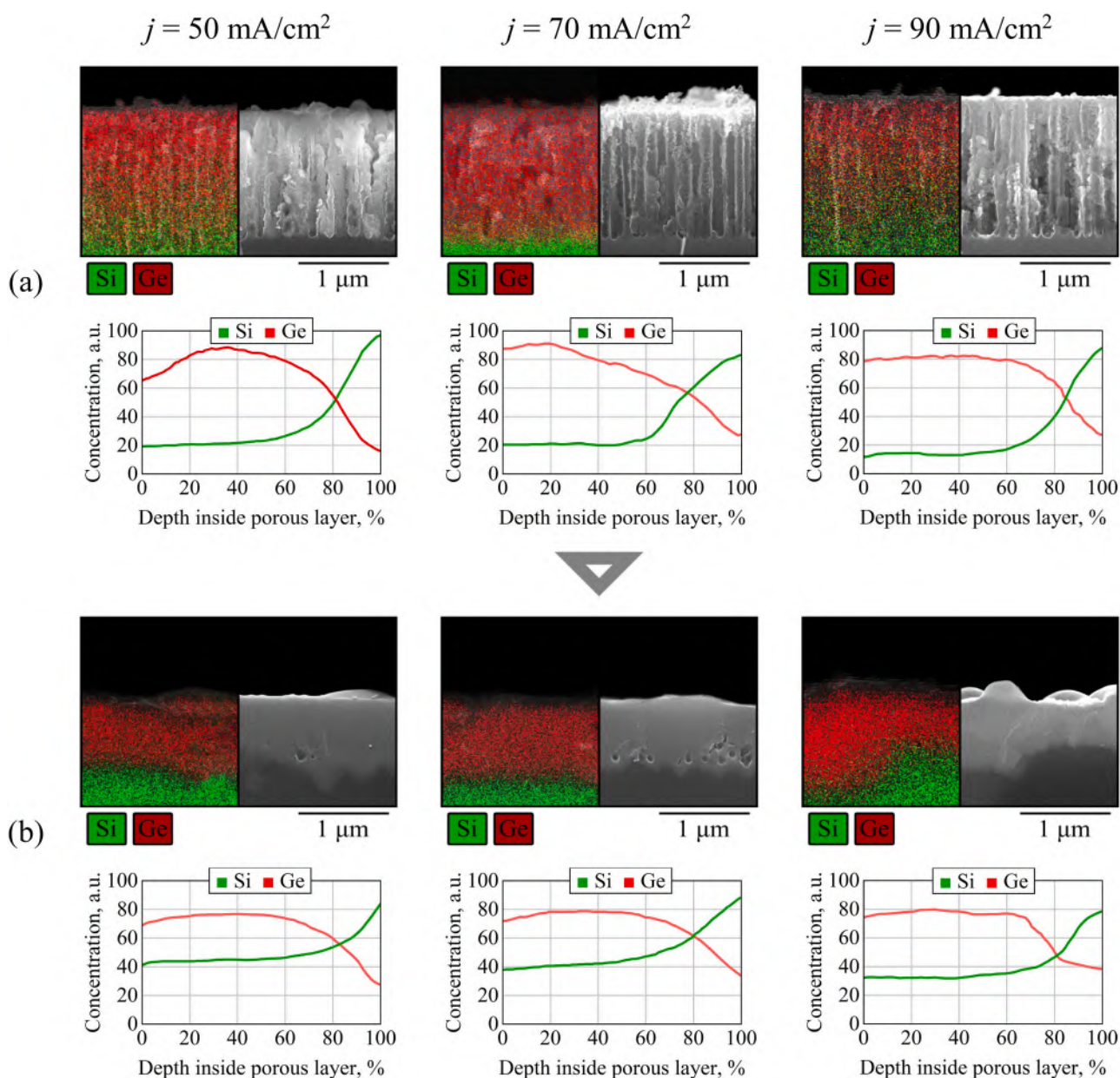
Fig. 2. Cross-section SEM images with corresponding EDX maps and element signature profiles of anodic PS samples prepared at three different anodization current densities *j* after (a) germanium deposition and (b) subsequent RTP.

annealing, indicating oxide formation during thermal processing. We currently attribute this to the presence of leftover oxygen inside the pores in various forms, including but not limited to hydroxy groups passivating the PS surface and residual water and deposition solution droplets trapped within the pores due to capillary action. Due to the lack or a pre-heating stage, these oxygen atoms are redistributed during RTP, resulting in oxide formation.

Most of the peaks listed are reproducibly present on all samples regardless of porosity and only vary in intensity. Particularly, the intensities of peaks inherent to germanium fractions generally become more pronounced along with an increase in matrix porosity, which would indicate a reduction in silicon content. On the other hand, the silicon oxide peak gradually increases along with porosity, which is attributed to an increased oxidation speed of the more developed PS surfaces obtained at higher current densities.

The samples' Raman spectra compiled in Fig. 4 exhibit three primary bands. The rightmost band at the wavenumber of 521 cm^{-1} corresponds to the triple-degenerate optical vibrational mode of monocrystalline silicon Si (LO) in the center of the Brillouin zone [30]. Naturally, this peak is present in most samples, apart from cases where a thick layer of excess germanium completely obstructs the sample's surface. The second band located at 300 cm^{-1} appears after germanium deposition and corresponds to the analogous vibrational mode of crystalline germanium Ge (LO). Both silicon and germanium bands are wider than those seen on pristine materials (Fig. 4, a), as their crystallinity is reduced due to pore formation. Subsequently to RTP, a third band appears in the spectrum, corresponding to the signature of a Si$_{1-x}$Ge$_x$ alloy. Additionally, the bands become more asymmetric, indicating possible manifestation of dimensional effects, defects, surface states, or non-stoichiometric material composition [31]. Notably, thermal processing also leads to a significant shift in the band associated with silicon (down to 496, 489 and 486 cm^{-1} for PS formed at 50, 70 and 90 mA/cm^2, respectively). Raman peak shifts such as these can occur for a variety of reasons, ranging from a change in doping to mechanical stress, and usually
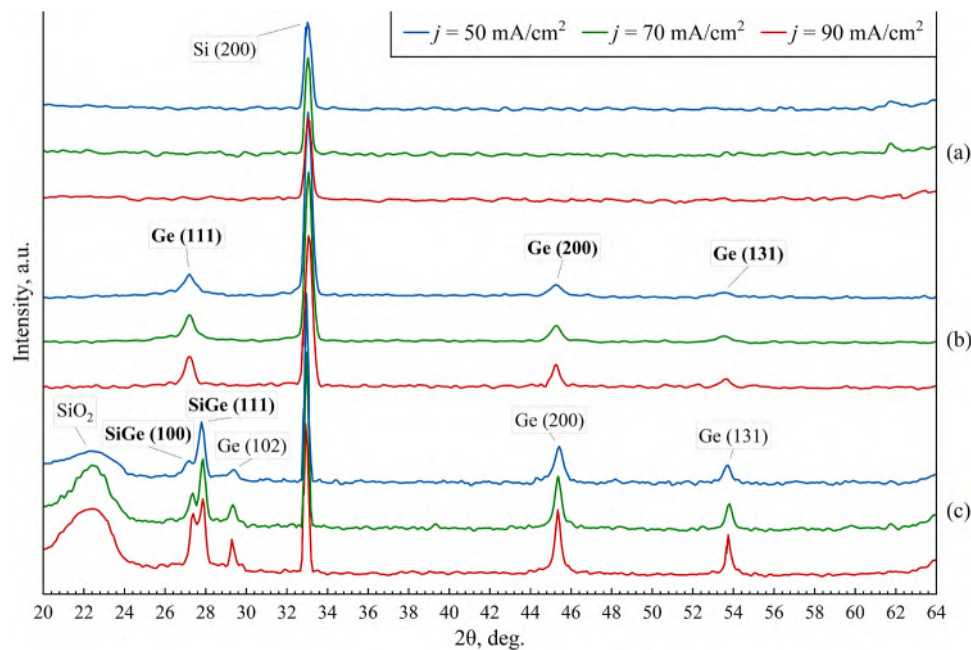
Fig. 3. XRD spectra of samples based on anodic PS prepared at three different anodization current densities *j*: (a) initial PS layers, (b) PS layers filled with germanium and (c) the same PS layers subjected to RTP.

indicate a change in crystallinity or defect density of the material in question [32]. In this case one can expect the shift to be caused by mechanical strain due to silicon and germanium lattice mismatch. In some cases, such as anodization at 70 mA/cm^2, the simultaneous presence of the original "unstrained" peak at 512 cm^{-1} may be caused by the accumulation of signals acquired on different crystal faces from differently-sized silicon particles, as well as the contribution of transverse optical (TO) phonons [33,34]. It is also slightly shifted from its original position at 521 cm^{-1} due to the aforementioned factors. All three primary peaks are present on alloyed samples regardless of their fabrication regimes, and indicate an increase in germanium concentration along with anodization current density *j*, which also correlates with XRD data.

3.2. Vertically-aligned silicon nanowires

Analogously to the previously presented results, Figs. 5–8 depict SEM images, as well as EDX, XRD and Raman spectroscopy data of three sample groups: initial SiNW array samples produced by MACE and filled with indium, SiNW samples filled with indium and germanium and, lastly, the same samples subjected to thermal processing.

First stage SEM images (Fig. 5, a) indicate formation of a silver mask consisting of interconnected nanoscale particles. During the MACE process, silver particles greatly facilitate etching rate of silicon directly underneath them — as such, the silver mask directly dictates the positions and sizes of pores and can be used to regulate the layer's porosity. Raising the silver deposition time leads an increase in particle size and, consequently, reduces the distance between particles and causes them to overlap, which in turn increases the porosity of structures obtained at the subsequent etching stage. SiNW layers formed at silver deposition times of 15, 30 and 60 s (Fig. 5, b) are characterized by, respectively, equivalent wire diameters of 90, 85 and 70 nm and average pore channel widths of 75, 100 and 145 nm. Nanoscale silver particles are present in their bottommost parts. Consequently, indium deposition conducted at the following stage (Fig. 5, b) is fully localized at the silver particles, resulting in cylindrical indium deposits up to 200 nm in height located precisely at the pore bottoms. Germanium growth (Fig. 5, c) then initiates there and proceeds uniformly throughout the porous layer, leading to adequate pore filling. The minor exception to that is the lack

of germanium in the subsurface layer, which can be attributed to adjacent SiNW bundling together, resulting in the presence of unfilled gaps. Similarly to the previous case, RTP results in the formation of alloyed layers (Fig. 5, d), possessing slightly reduced thicknesses in relation to those of the original SiNW arrays. The samples in question are presented in more detail in Fig. 6. Notably, EDX signatures for silver and indium are nearly non-existent after RTP, possibly indicating their redistribution throughout the newly formed layer.

As can be derived from XRD spectra compiled in Fig. 7, the silicon and germanium XRD peaks observed before RTP are nearly identical to those seen in the case of anodic PS. Notably, peaks characteristic of pure indium [35,36] and silver [37,38] are non-existent subsequently to indium and germanium deposition, and instead signatures associated with In$_4$Ag$_9$ (411), (332) and (600) (37°, 41.5° and 57.6°) [39], as well as InAg$_3$ (220) (60.3°) [40] emerge, indicating a certain degree of indium-silver alloying. The latter is known as a possible outcome of forming indium deposits on silver substrates due to mutual intermetallic diffusion [41]. Subsequently to RTP, peaks associated with additional germanium crystalline configurations arise, including Ge (111), (102), (131) and (112) (34°). Additionally, peaks characteristic of the Si$_{1-x}$Ge$_x$ become apparent, namely SiGe (100) (27.3°), SiGe (111) (27.8°), SiGe (112) (38.6°), SiGe (004) (39.3°), SiGe (200) or (220) (46.2°) and SiGe (131) (55°), the latter four unpresented in anodic PS [26,27]. At the same time, the wide peak associated with SiO$_2$ is much less pronounced, which can most likely be attributed to defect-free surface of SiNWs, making them less prone to oxidation.

The samples' Raman spectra compiled in Fig. 8 bear little to no qualitative difference in comparison to their counterparts registered on anodic PS, including the positions of peaks associated with silicon (496, 493 and 486 cm^{-1} for SiNWs formed at t_{Ag} = 15, 30 and 60 s, respectively). The "unstrained" peak is also present for t_{Ag} = 15, with its position shifted to the value of 511 cm^{-1}.

3.3. Comparison and discussion

While the two porous matrix types are visually similar, the primary morphological differences between them are the relatively smooth defect-free surface and the lack of interconnections between pore sidewall elements in the case of SiNWs which generally comprise isolated
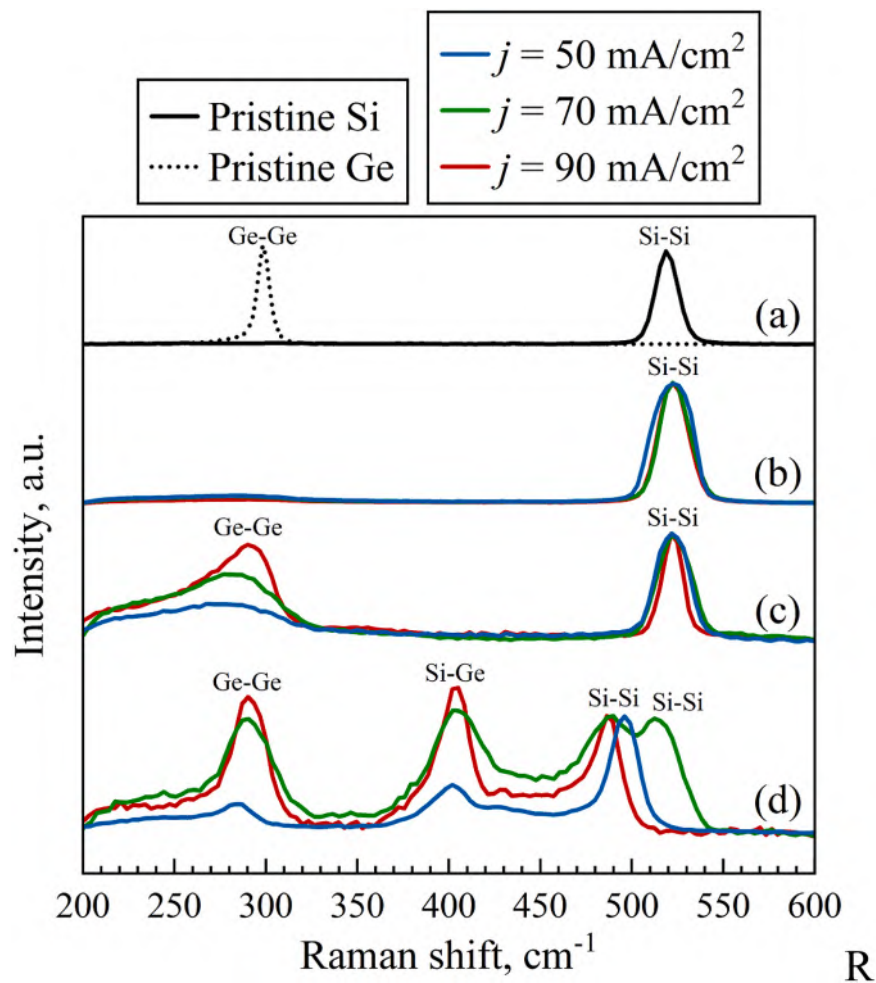
Fig. 4. Raman spectra of samples based on anodic PS prepared at three different anodization current densities *j*: (a) monocrystalline Si (100) and Ge (100) wafers for reference, (b) initial PS layers, (c) PS layers filled with germanium and (d) the same PS layers subjected to RTP. Peak intensity is normalized to monocrystalline silicon's band.

vertically-aligned wires. Germanium deposition into either type of porous matrix yields fairly similar results in terms of the germanium deposits' crystalline structure. The latter is generally present in its (111) and (200) cubic crystalline forms. Apart from silver and indium XRD signatures (Fig. 7, b), the minor distinctions between the two matrix types are the presence of a weakly pronounced peak associated with Ge (112) in the case of MACE-produced SiNWs, as well as the overall difference in peak intensities corresponding to each crystalline phase. This likely stems from slight differences in germanium's growth mechanism. For anodic PS it is strictly limited to standard liquid-phase electrodeposition kinetics, where germanium nucleation occurs ubiquitously along the pore sidewalls. In the case of indium-filled SiNWs it's expected that the process would also incorporate simultaneous occurrence of ec-LLS growth of germanium inside each fusible metal particle.

The difference in germanium nucleation density on the sidewalls can be attributed to two factors: the well-developed rough surface of anodic PS and the use of heavily-doped silicon, both greatly promoting deposition conformity. The abundance of defects and doping atoms present in anodic PS enables a significantly increased nucleation density, followed by continuous growth and uniform pore filling. In the case of SiNWs, sidewall nucleation is inhibited by the lack of both defects (as the wire surface is very smooth) and doping atoms (as lightly-doped wafers are used), resulting in fewer nuclei. As a result, semiconductor nucleation primarily occurs on the surface or in the volume of indium particles present in the bottommost parts of the pores in accordance with the ec-LLS mechanism. During ec-LLS the fusible metal particles

simultaneously act as microscopic cathodes (electron sources) whereat the oxidized semiconductor precursor (GeO$_2$) is electrochemically reduced to a zero-valent state and as nucleation points [16]. As a result, semiconductor crystal growth occurs underneath each metal particle, usually pushing the latter upwards as the process goes on and forming a semiconductor wire directly below it. Constricted by the sidewalls, the germanium wire then proceeds to fill the pore from its bottom to its top. Due the growth mechanism being strongly directional and independent on diffusion limitations, unfilled voids are expected to be present on a lesser degree compared to anodic PS.

Evidently, the pore filling approach becomes largely insignificant after RTP, emanating in the formation of a uniform Si$_{1-x}$Ge$_x$ layer in either case. This in term causes additional XRD peaks to emerge, associated with various crystalline forms of Si$_{1-x}$Ge$_x$. Key differences between approaches to SiGe fabrication using anodic PS and SiNWs are illustrated by Fig. 9.

For the ease of comparison, experimental data obtained at different PS layer fabrication regimes are compiled in Table 1. The porosity and layer thickness values were determined based on surface and cross-section image analysis, which in the case of anodic PS was performed using images obtained after subsurface layer removal. The alloy's composition was estimated based on the bands' intensities. It should be noted that Raman scattering from Si$_{1-x}$Ge$_x$ contributes to all three peaks. As such, their intensities do not directly correspond to silicon and germanium fractions and are instead used for indirect calculation. Supposing the random distribution of silicon and germanium atoms in
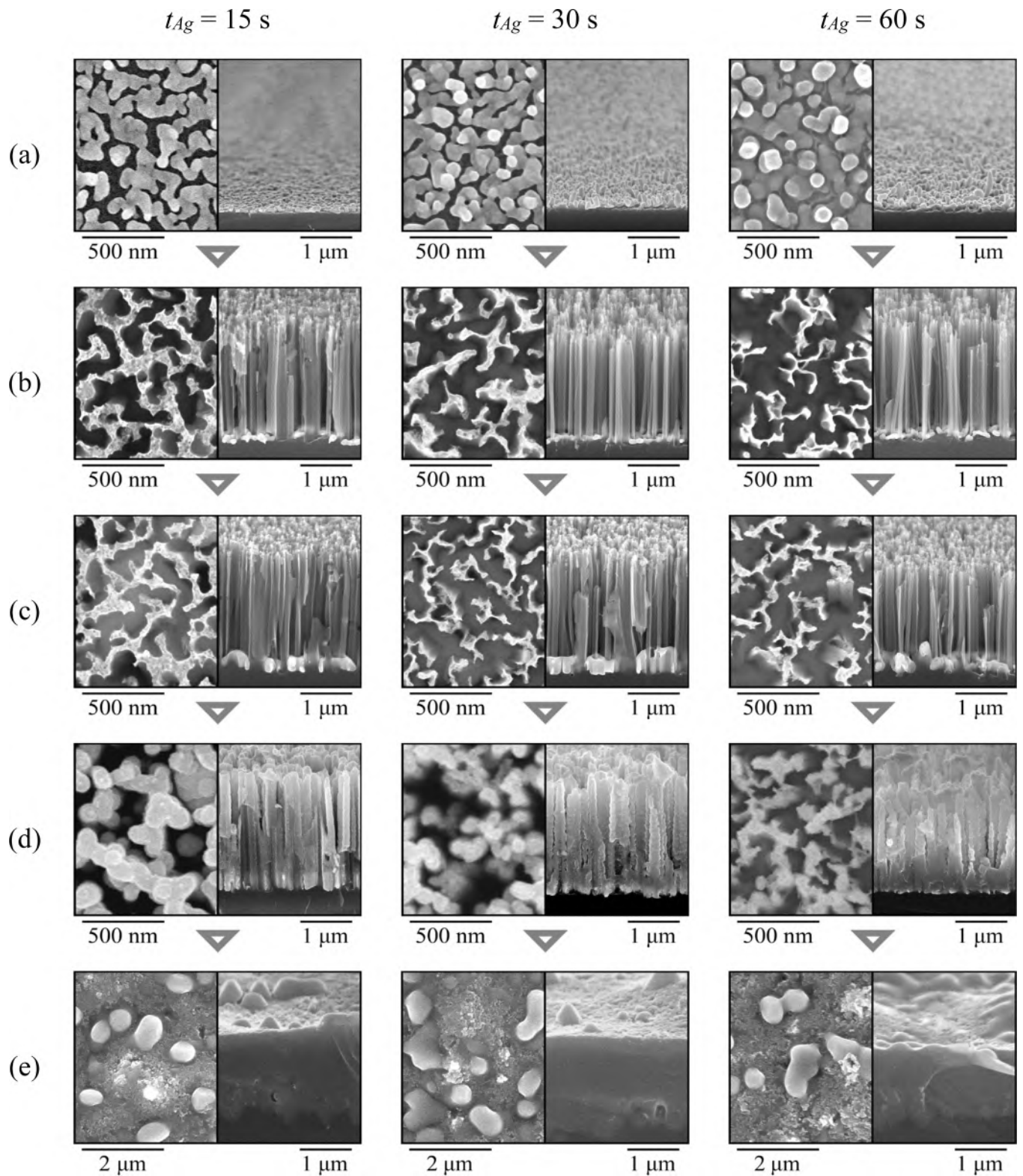
Fig. 5. Surface and bird's-eye view SEM images of samples prepared on the basis of MACE with varying silver mask deposition times t$_{Ag}$: (a) initial silver mask, (b) SiNWs resulting from MACE, (c) SiNWs filled with indium, (d) SiNWs filled with indium and germanium and (e) the resulting samples subjected to RTP.

Si$_{1-x}$Ge$_x$, one can assume that the probability of bond formation by Ge-Ge, Si-Ge, and Si-Si is close to x^2, $2x(1 - x)$, and $(1 - x)^2$, respectively. Band intensity I (a.u.) is proportional to the number of corresponding chemical bonds. The ratios of band intensities related to these bonds can then be written as follows [30]:

$$I_{Ge-Ge}/I_{Si-Ge} = Bx/2(1-x), \qquad (2)$$

$$I_{Si-Si}/I_{Si-Ge} = A(1-x)/2x. \qquad (3)$$

The coefficients A and B are implemented to account for resonance effects resulting in the dependence of band intensity on excitation
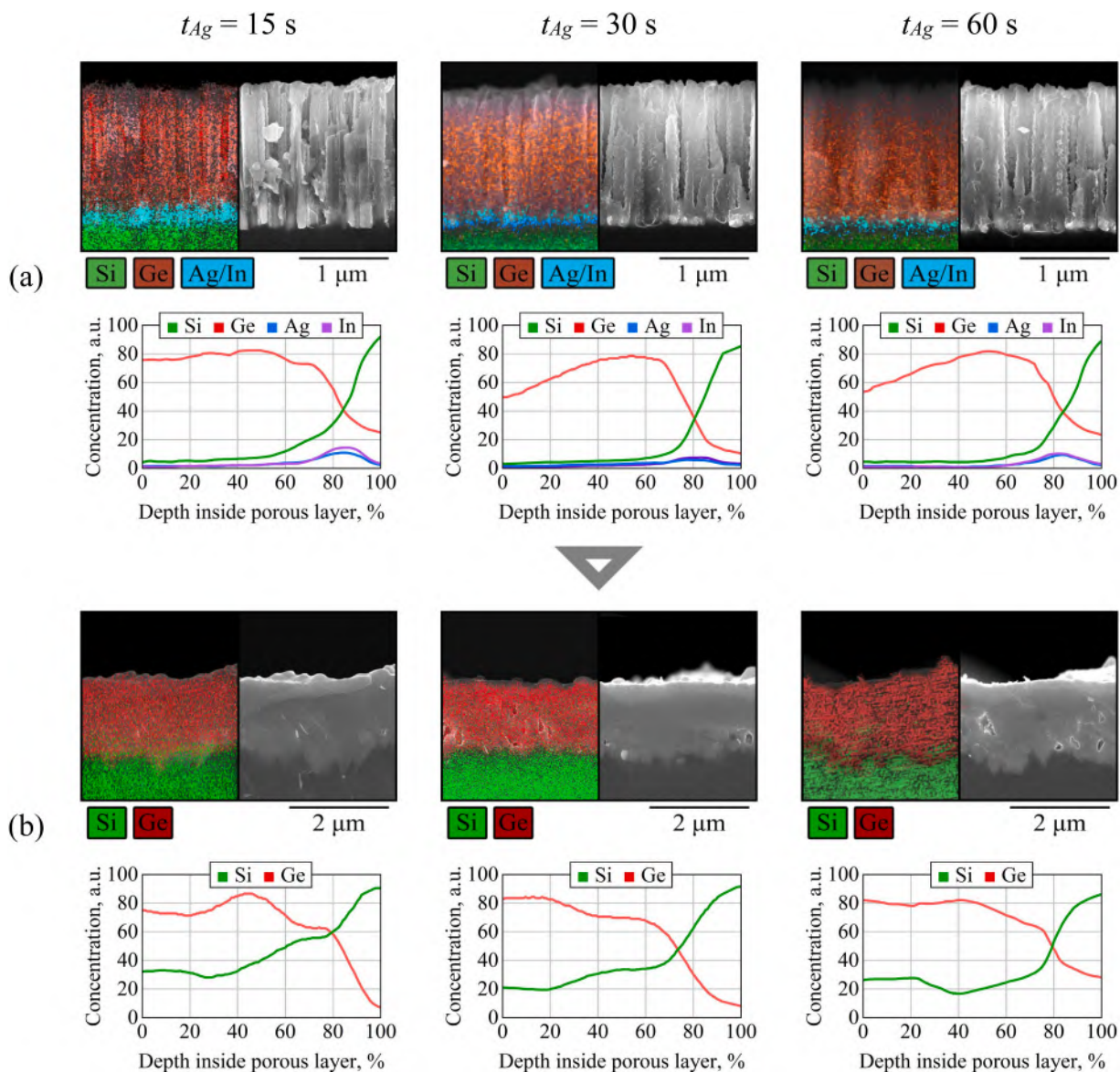
Fig. 6. Cross-section SEM images with corresponding EDX maps and element signature profiles of SiNWs prepared at varying silver mask deposition times t_{Ag} after (a) germanium deposition and (b) subsequent RTP.

wavelength. Based on the ratio of band intensities, germanium's concentration in the alloy can be estimated independently of mechanical stresses. It is assumed that an excess of germanium in the resulting material is present, and the corresponding Ge-Ge bond in the Raman spectrum incorporates the signal of both pure germanium and the alloy. At the same time, the Si-Ge and Si-Si bands can only correspond to the alloy. Therefore, using the experimental coefficients A and B from [30] and expression (3), the x values for germanium fractions in the resulting $Si_{1-x}Ge_x$ alloys were obtained, suggesting alloy compositions of $Si_{0.69}Ge_{0.31}$, $Si_{0.28}Ge_{0.72}$ and $Si_{0.17}Ge_{0.83}$ for PS prepared at 50, 70 and 90 mA/cm^2, respectively.

Both types of PS exhibit a significant effect of matrix porosity on the resulting alloy's composition. While an increase in porosity, as expected, generally leads to a decrease in silicon content, this dependency varies in steepness for the two sample types. A ~70% porosity value yields similar $Si_{1-x}Ge_x$ compositions for either type of PS ($x \approx 0.72$); however, at the 66% mark a drastic decrease in germanium content ($x \approx 0.31$) is observed for anodic PS, much more significant than that in MACE-produced samples ($x = 0.71$ at 68%). Presumably, this is caused by major differences in morphology between anodic PS and SiNWs at the

same porosity value and the specific mechanisms of pore filling inherent to each matrix type. Namely, growth of germanium inside SiNWs proceeds in accordance with the ec-LLS mechanism and fills the pore vertically from bottom to top, minimizing unfilled voids and leading to increased germanium contents at the same porosity value as in anodic PS. The exact distinctions in the alloying mechanism are currently under investigation.

Otherwise, both anodic PS and SiNWs produced by MACE are characterized by their specific traits. In accordance with hot-point probe measurements, the alloy inherits the doping type of whichever wafer it is prepared on. Considering the above, the two fabrication approaches have to be compared primarily based on the porous morphology range they are able to provide, the applicable substrate dopants and their concentrations, as well as their overall ease of implementation. MACE provides a more limited selection of porous morphologies that can be produced, as the only means to regulating porosity is changing the silver deposition time. This can be amended by utilizing lithography to apply silver in a pre-defined pattern, but at the cost of significantly complicating the manufacturing process. Additionally, as MACE results are strongly dependent on surface quality, great care should be taken during
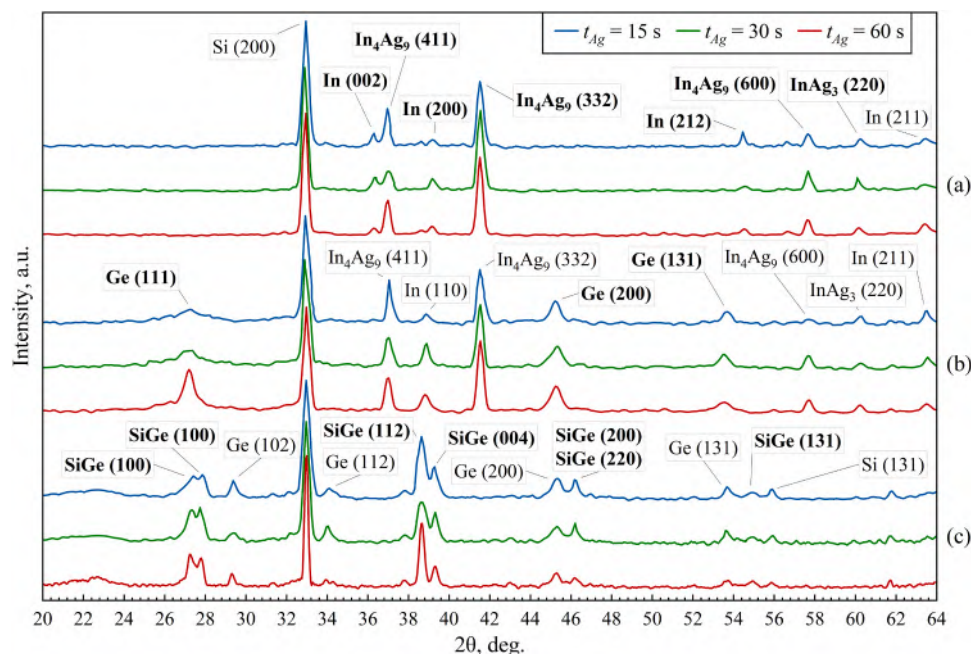
Fig. 7. XRD spectra of samples prepared on the basis of MACE with varying silver mask deposition times t_{Ag}: (a) initial SiNWs with indium deposits, (b) the same SiNWs filled with germanium and (c) the same samples after RTP.

wafer preprocessing and immersion to achieve reproducible results. Another obvious drawback is the very need to use silver and indium — both rather expensive metals — in the first place, as well as their presence in the resulting silicon-germanium alloys. Presumably, however, the latter factor can also serve as a situational advantage, as the metals in question can take on the roles of dopants. Lastly, SiNW layers consisting of wires with excessive aspect ratios (usually with lengths above 20 μm) may be subject to significant deformation or breakdown during germanium deposition due to a combination of high temperatures and stirring. This puts a hard limit on the range of alloy thicknesses attainable.

Using anodic PS allows for a much less complex approach without the need for many additional processing stages and enables fabrication of layer thicknesses greatly surpassing the limitations of SiNW arrays. Another beneficial factor is the well-documented ability to form a large variety of porous morphologies by altering the anodization regimes (current density and etching solution composition). However, the ability to reproducibly form anodic PS layers may be hindered by the difference in anodization mechanism for wafers with different conductivity types, dopant concentrations and crystal orientations. Additionally, not every single structural type of PS can be expected to produce satisfactory results in terms of germanium filling. As such, a combination of either type of process may be required for differently-doped SiGe structures to be formed. Based on our preliminary results, both p- and n-type heavily-doped wafers can be used for anodic PS preparation and subsequent germanium filling and alloying, yielding p- and n-type $Si_{1-x}Ge_x$ layers with high dopant concentrations. Similarly to this, lightly-doped alloys of either conductivity type can be easily produced based on SiNWs prepared by MACE of lightly-doped p- and n-type silicon wafers. However, fabrication of anodic PS on lightly-doped wafers and SiNWs on heavily-doped wafers has not yet been evaluated and requires further confirmation.

It should be noted that Raman spectroscopy provides information solely on the surface and subsurface layers of the material. As indicated by EDX concentration spectra, lateral composition may significantly deviate from these values and should be clarified with the use of a more adaptable technique.

3.4. Electrophysical parameters

The primary difficulty of studying electrophysical properties of thin films formed on conductive substrates lies in taking into account the input of the underlying substrate. As such, substrates with the lowest possible electrical conductivity are usually employed for their preparation, which is impossible in this case due to the use of doped silicon as a base for PS formation. The substrate's contribution to electrical conductivity can be estimated by interpreting the film/substrate system as two conductors connected in parallel. The sample's Seebeck coefficient S can then be defined as

$$S_T = (S_f \cdot \sigma_f + S_s \cdot \sigma_s)/\sigma_T, \tag{4}$$

$$\sigma_T = (\sigma_f \cdot d_f + \sigma_s \cdot d_s)/(d_f + d_s), \tag{5}$$

where σ is the specific electrical conductivity, and d is the layer thickness. The index f refers to the film, s to the substrate, and T to the sample in its entirety.

The temperature dependencies of various electrophysical parameters of pristine lightly-doped p-type silicon, as well as those of the $Si_{0.29}Ge_{0.71}$ alloy sample (subsequently referred to simply as "sample") prepared thereon using MACE-formed SiNWs with $t_{Ag} = 60$ s are presented in Fig. 10. Accompanying them are the theoretical data for the isolated alloyed film obtained using expressions (4) and (5). The power factor value was calculated as σS^2.

Notably, the pristine substrate's resistance is greater than that of the sample over the whole temperature range, suggesting the viability of the bilayer model. The Seebeck coefficient is positive at room temperature, indicating p-type electrical conductivity. These results are consistent with the data reported by N. Hirashita et al. [42], who showed that samples with $x > 0.4$ exhibit p-type conductivity. The film resistivity calculation at room temperature with the use of (5) gives a value of 6 Ohm·cm, which is 40 times higher than the result reported in [42] for $x = 0.7$. This difference most likely stems from additional scattering of carriers at the film's intergranular boundaries.

The resistivity-temperature curve behavior (Fig. 10, b) corresponds to that of a moderately-doped semiconductor. An increase in resistivity at temperatures up to 500 K is associated with a decrease in charge
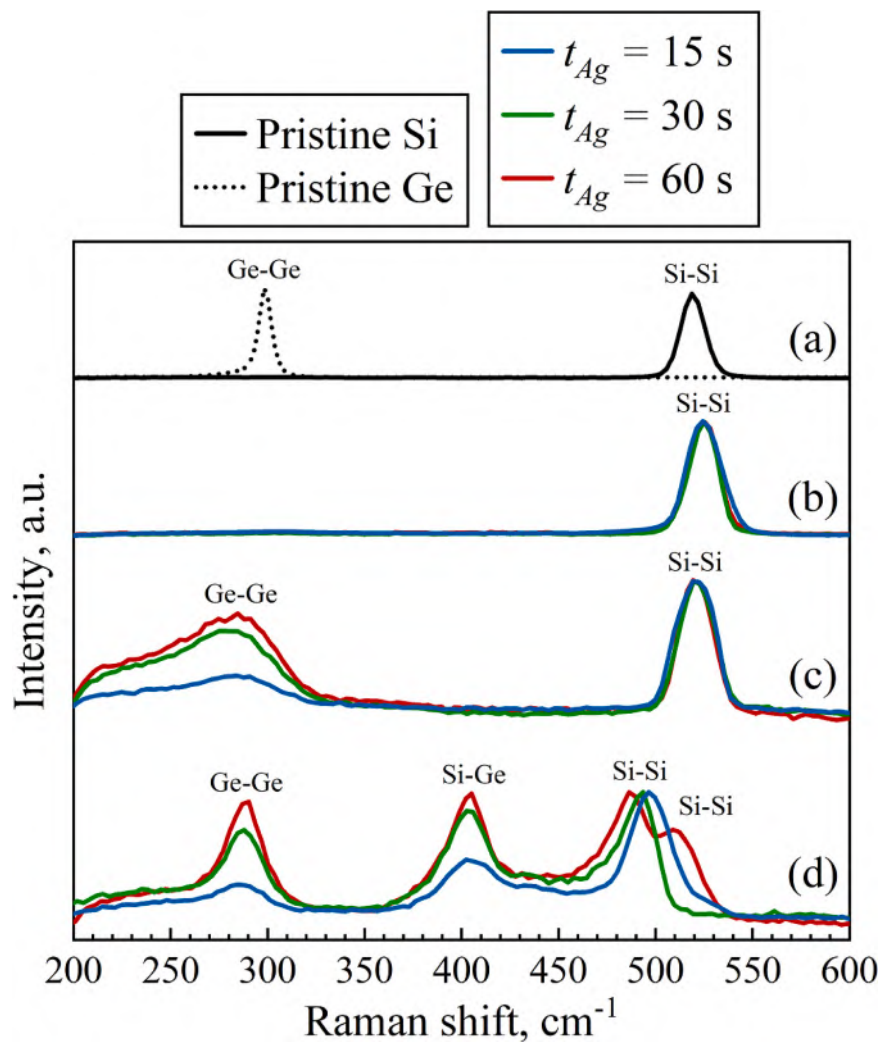
Fig. 8. Raman spectra of samples prepared on the basis of MACE with varying silver mask deposition times t_{Ag}: (a) monocrystalline Si (100) and Ge (100) wafers for reference, (b) initial SiNWs with indium deposits, (c) SiNWs filled with germanium and (d) the same samples subjected to RTP. Peak intensity is normalized to monocrystalline silicon's band.

carrier mobility due to phonon scattering. The concentration of charge carriers in this range remains practically unchanged, as all doping atoms are already ionized. However, as the temperature is increased, the generation of intrinsic charge carriers at interband transitions is initiated, and the semiconductor enters the intrinsic conductivity region, accompanied by a decrease in resistivity. The concentrations of electrons and holes begin to equalize, which is reflected in the decrease of the Seebeck coefficient (Fig. 10, c). However, since the mobility of electrons is greater than that of holes and p-type silicon is used, the sign of thermal voltage changes from positive to negative. The temperature at which this change occurs depends on the concentration of holes in the semiconductor, and the larger it is, the higher the temperature at which the Seebeck coefficient becomes negative. The higher concentration of holes in the film compared to the substrate is reflected in the rapid decrease in film resistivity and the Seebeck coefficient becoming negative at T = 550–850 K (Fig. 10, b, c).

At temperatures below 550 K, in the extrinsic conductivity region, the film's Seebeck coefficient reaches values up to 3 mV/K. This is significantly higher than the data reported in literature, which may be due to the low concentration of charge carriers in the film. At temperatures above 580 K, the sign of the Seebeck coefficient is determined by the more mobile electrons, and its value slightly differs from the substrate, which can be attributed to the transition into the intrinsic conductivity region. The values of S_s and σ_s obtained from (4) and (5) were

used to calculate the power factor of the film (Fig. 10, d). It varies slightly from 120 $\mu W \cdot m^{-1} \cdot K^{-2}$ at 330 K to 390 $\mu W \cdot m^{-1} \cdot K^{-2}$ at 850 K, except for a decrease at 530–630 K due to the change in majority charge carriers in the film. These results are attributed to the high Seebeck coefficient, as well as high resistance in the extrinsic region and low resistance and Seebeck coefficient in the intrinsic region. The registered power factor value is lower than that reported in literature, which is explained by the relatively low electrical conductivity of the film even at 850 K. Presumably, it is possible to increase the electrical conductivity value by utilizing more highly-doped silicon for alloy preparation or, alternatively, by depositing the dopant prior to to the annealing stage. This possibility, as well as the impact of PS matrix porosity and alloy composition on its thermoelectric properties are currently under investigation.

4. Conclusions

Based on SEM, EDX, XRD and Raman spectroscopy results, it can be concluded that the proposed method enables fabrication of various $Si_{1-x}Ge_x$ alloy layers, with their thickness directly corresponding to that of the initial porous layer and the composition dependent on the porosity of the PS layer used as a structural matrix. Altering the initial matrices' porosity values by varying the anodization current density (for anodic PS) or the silver mask deposition time (for MACE-produced layers)
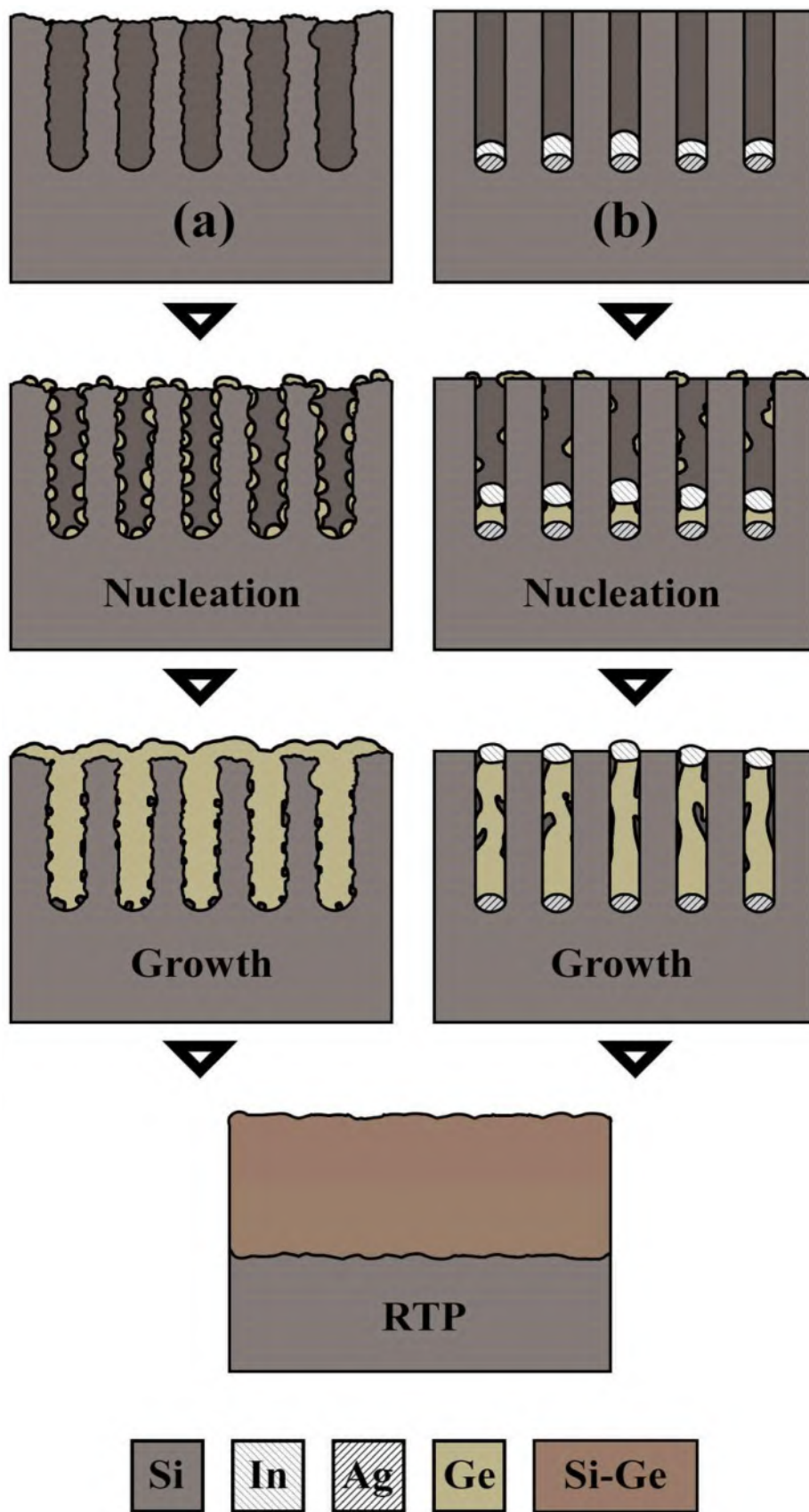
Fig. 9. Schematic illustration of the germanium nucleation and growth process in the case of utilizing (a) anodic PS and (b) MACE-produced SiNWs.

Table 1
Summary of the experimental samples' physical parameters.

Type of porous matrix	Porosity, %	Porous matrix layer thickness, μm	Resulting alloy layer thickness, μm	Resulting alloy composition
Anodic PS, $j = 50$ mA/cm^2	66	1.19	0.76	$Si_{0.69}Ge_{0.31}$
Anodic PS, $j = 70$ mA/cm^2	70	1.08	0.75	$Si_{0.28}Ge_{0.72}$
Anodic PS, $j = 90$ mA/cm^2	75	1.36	0.68	$Si_{0.17}Ge_{0.83}$
SiNWs, $t_{Ag} = 15$ s	55	2.20	1.70	$Si_{0.68}Ge_{0.32}$
SiNWs, $t_{Ag} = 30$ s	63	2.08	1.68	$Si_{0.44}Ge_{0.56}$
SiNWs, $t_{Ag} = 60$ s	68	1.98	1.55	$Si_{0.29}Ge_{0.71}$

enables direct control over silicon and germanium fractions in the resulting alloy, as indicated by the change of x in $Si_{1-x}Ge_x$ from 0.31 to 0.83 as the porosity value is changed from 55 to 75%. While both types of matrices exhibit an increase in germanium contents along with porosity, the difference is not directly tied to its value, but also changes depending the type of matrix used, as indicated by major changes in alloy compositions obtained on different PS types at the same porosity levels. The exact cause of this is currently under investigation. Otherwise, the choice between anodic PS and SiNWs produced by MACE is scarcely reflected in resulting alloy layer's crystalline structure and comes down to the choice between available porous morphologies and the resulting alloy's doping types, as the latter appear to be directly inherited from the substrate.

Prime Novelty Statement

In this paper, we further elaborate upon the previously proposed new approach to forming silicon-germanium ($Si_{1-x}Ge_x$) alloy layers based on porous silicon matrices by electrochemically filling the latter with germanium and annealing the as-prepared structure under specific conditions. Resulting from this procedure are relatively uniform $Si_{1-x}Ge_x$
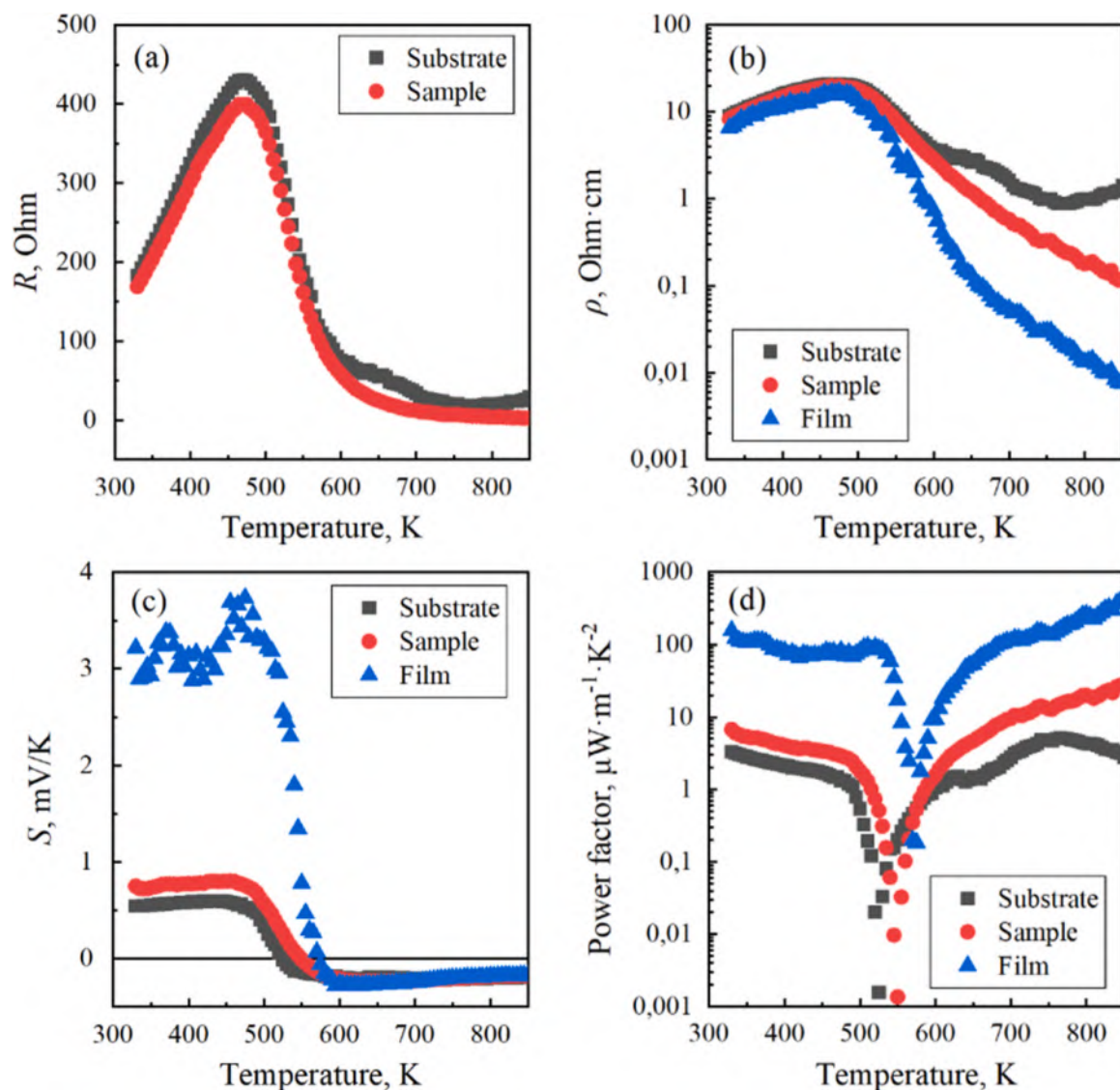
Fig. 10. Temperature dependence of (a) resistance R, (b) resistivity ρ, (c) Seebeck coefficient S and (d) power factor for (black) the initial p-Si substrate, (red) the same substrate with a Si-Ge alloy film on its surface and (blue) the isolated film.

layers located on monocrystalline silicon with their thicknesses directly corresponding to those of the original porous matrices. The prime novelty of this particular research is the established possibility to directly control the alloy's composition (i.e., the fractions of silicon and germanium in $Si_{1-x}Ge_x$) by adjusting the porosity values of each given porous matrix. While such a possibility was theoretically considered in our previous works on the subject, this is the first time it has been experimentally confirmed.

Funding

CRediT authorship contribution statement

Bondarenko Vitaly: Conceptualization, Data curation, Formal analysis, Project administration, Supervision, Validation, Writing – review & editing. **Chubenko Eugene:** Data curation, Formal analysis, Validation. **Dronov Alexey:** Project administration, Resources. **Gavrilin Ilya:** Formal analysis, Funding acquisition, Resources. **Grevtsov Nikita:** Formal analysis, Investigation, Methodology, Validation, Visualization, Writing – original draft. **Argunov Efim:** Investigation. **Yanushkevich Kazimir:** Resources, Software. **Rymski Grigory:** Investigation, Resources, Software. **Gavrilov Sergey:** Project administration, Resources. **Goroshko Dmitry:** Investigation.

Declaration of Competing Interest

The authors declare that they have no known competing financial interests or personal relationships that could have appeared to influence the work reported in this paper.

Data Availability

Data will be made available on request.

Acknowledgments

References

[1] R. Basu, A. Singh, High temperature Si–Ge alloy towards thermoelectric applications: a comprehensive review, Mater. Today Phys. 21 (2021), 100468, https://doi.org/10.1016/j.mtphys.2021.100468.

[2] B. Cook, Silicon-germanium: the legacy lives on, Energies 15 (2022) 2957, https://doi.org/10.3390/en15082957.

[3] K. Xie, M. Gupta, Thermoelectric properties of SiGe thin films prepared by laser sintering of nanograin powders, J. Alloy. Compd. 820 (2019), 153182, https://doi.org/10.1016/j.jallcom.2019.153182.

[4] C. Schwinge, K. Kuhnel, J. Emara, L. Roy, K. Biedermann, W. Weinreich, S. Kolodinski, M. Wiatr, G. Gerlach, M. Wagner-Reetz, Optimization of LPCVD phosphorous-doped SiGe thin films for CMOS-compatible thermoelectric applications, Appl. Phys. Lett. 120 (2022), 031903, https://doi.org/10.1063/5.0076945.

[5] F. Lange, O. Ernst, T. Teubner, T. Boeck, Investigation of Au droplet formation and growth of SixGe1−x nanowires by molecular beam epitaxy, CrystEngComm 22 (2020) 6322.

[6] C. Littlejohns, Next Generation Device Grade Silicon-Germanium on Insulator, Sci. Rep. 5 (2015) 8288.

[7] J. Taborda, J. Romero, B. Abad, M. Munoz-Rojo, A. Mello, F. Briones, M. Gonzalez, Low thermal conductivity and improved thermoelectric performance of nanocrystalline silicon germanium films by sputtering, Nanotechnology 27 (2016), 175401.

[8] M. Isomura, M. Yajima, I. Nakamura, Crystallization of silicon–germanium by aluminum-induced layer exchange, Jpn. J. Appl. Phys. 57 (2018), 025503, https://doi.org/10.7567/JJAP.57.025503.

[9] A. Uhlir, Electrolytic Shaping of Germanium and Silicon, Bell Syst. Techn. J. 35 (1956) 333, https://doi.org/10.1002/j.1538-7305.1956.tb02383.x.

[10] G. Korotcenkov (Ed.), First ed..,Porous Silicon: From Formation to Application: Formation and Properties, Volume One, CRC Press, Boca Raton, 2016 doi:10.1201/b19342.

[11] L. Canham (Ed.), Handbook of Porous Silicon, Second ed., Springer, 2014.

[12] H. Bandarenka, A. Dolgiy, E. Chubenko, S. Redko, K. Girel, S. Prischepa, A. Panarin, S. Terekhov, V. Pilipenko, V. Bondarenko, Nanostructured metal films formed onto porous silicon template, J. Nano. Res. 39 (2016) 235, https://doi.org/10.4028/www.scientific.net/JNanoR.39.235.

[13] N. Vorozov, L. Dolgyi, V. Yakovtseva, V. Bondarenko, M. Balucani, G. Lamedica, A. Ferrari, G. Vitrant, J. Broquin, T. Benson, H. Arrand, P. Sewell, Self-aligned oxidised porous silicon optical waveguides with reduced loss, Electron. Lett. 26 (2000) 722, https://doi.org/10.1049/el:20000490.

[14] V. Yakovtseva, L. Dolgyi, N. Kazuchits, N. Vorozov, M. Balucani, V. Bondarenko, L. Franchina, G. Lamedica, A. Ferrari, Oxidized porous silicon: from dielectric isolation to integrated optical waveguides, J. Porous Mater. 7 (2000) 215, https://doi.org/10.1023/A:1009647007232.

[15] E. Chubenko, S. Redko, A. Dolgiy, H. Bandarenka, S. Prischepa, V. Bondarenko, Porous Silicon as Host and Template Material for Fabricating Composites and Hybrid Materials, doi: 10.1201/b19042–12.

[16] N. Grevtsov, E. Chubenko, V. Petrovich, V. Bondarenko, I. Gavrilin, A. Dronov, S. Gavrilov, Selective electrochemical deposition of indium in-between silicon nanowire arrays fabricated by metal-assisted chemical etching, Materialia 21 (2022), 101337, https://doi.org/10.1016/j.mtla.2022.101337.

[17] N. Grevtsov, E. Chubenko, V. Petrovich, V. Bondarenko, I. Gavrilin, A. Dronov, S. Gavrilov, Germanium electrodeposition into porous silicon for silicon-germanium alloying, Materialia 26 (2022), 101558, https://doi.org/10.1016/j.mtla.2022.101558.

[18] I.M. Gavrilin, N.L. Grevtsov, A.V. Pavlikov, A.A. Dronov, E.B. Chubenko, V. P. Bondarenko, S.A. Gavrilov, A new approach for producing of film structures based on Si1-xGex, Mater. Lett. 313 (2022), 131802, https://doi.org/10.1016/j.matlet.2022.131802.

[19] Y. Peng, L. Miao, J. Gao, C. Liu, M. Kurosawa, O. Nakatsuka, S. Zaima, Realizing high thermoelectric performance at ambient temperature by ternary alloying in polycrystalline $Si_{1−x-y}Ge_xSn_y$ thin films with boron ion implantation, Sci. Rep. 9 (2019), 14342, https://doi.org/10.1038/s41598-019-50754-4.

[20] A.R. Chelyadinsky, A.M. Dorofeev, N.M. Kazuchits, S. La Monica, S.K. Lazarouk, G. Maiello, G. Masini, N.M. Penina, V.F. Stelmakh, V.P. Bondarenko, A. Ferrari, Deformation of porous silicon lattice caused by absorption/desorption processes, J. Electrochem. Soc. 144 (1997) 1463, https://doi.org/10.1149/1.1837612.

[21] H. Bandarenka, S. Prischepa, R. Fittipaldi, A. Vecchione, P. Nenzi, M. Balucani, V. Bondarenko, Comparative study of initial stages of copper immersion deposition on bulk and porous silicon, Nanoscale Res. Lett. 8 (2013), 85, https://doi.org/10.1186/1556-276X-8-85.

[22] M. Haeri, ImageJ plugin for analysis of porous scaffolds used in tissue engineering, J. Open Res. Softw. 3 (2015) 1, https://doi.org/10.5334/jors.bn.

[23] P. Zaumseil, High-resolution characterization of the forbidden Si 200 and Si 222 reflections, J. Appl. Cryst. 48 (2015) 528, https://doi.org/10.1107/S1600576715004732.

[24] M. Nabil, Photoluminescence emission control of porous silicon, Soft Nano. Lett. 9 (2019) 35, https://doi.org/10.4236/snl.2019.93003.

[25] S. Goriparti, E. Miele, A. Scarpellini, S. Marrass, M. Prato, A. Ansaldo, F. De Angelis, L. Manna, R. Zaccaria, C. Capiglia, Germanium nanocrystals-MWCNTs composites as anode materials for lithium ion batteries, ECS Trans. 62 (2014) 19, https://doi.org/10.1149/06201.0019ecst.

[26] V. Aggarwal, A. Ghatak, D. Kanjilal, D. Kabiraj, A. Singha, S. Bysakh, S. Medda, S. Chakraborty, Fabrication of Germanium-on-insulator in a Ge wafer with a crystalline Ge top layer and buried GeO2 layer by oxygen ion implantation, Mat. Sci. Eng. B. 260 (2020), 114616, https://doi.org/10.1016/j.mseb.2020.114616.

[27] S. Batula, M. Jayasimhadri, A. Dhar, Mechanical properties and microstructure of spark plasma sintered nanostructured p-type SiGe thermoelectric alloys, Mater. Des. 87 (2015) 414, https://doi.org/10.1016/j.matdes.2015.08.017.

[28] R. Nandanwar, P. Singh, F. Haque, Synthesis and characterization of SiO2 nanoparticles by sol-gel process and its degradation of methylene blue, Am. Chem. Sci. J. 5 (2015) 1, https://doi.org/10.9734/ACSJ/2015/10875.

[29] W. Wu, X. Zou, Q. Li, B. Liu, R. Liu, D. Liu, Z. Li, W. Cui, Z. Liu, D. Li, T. Cui, G. Zou, Simple synthesis and luminescence characteristics of PVP-capped GeO2 nanoparticles, J. Nanomat. 2011 (2011), 841701, https://doi.org/10.1155/2011/841701.

[30] S.A. Mala, L. Tsybeskov, D.J. Lockwood, X. Wu, J.-M. Baribeau, Raman scattering in Si/SiGe nanostructures: revealing chemical composition, strain, intermixing, and heat dissipation, J. Appl. Phys. 116 (2014), 014305, https://doi.org/10.1063/1.4886598.

[31] Y. Gao, P. Yin, Origin of asymmetric broadening of Raman peak profiles in Si nanocrystals, Sci. Rep. 7 (2017), 43602, https://doi.org/10.1038/srep43602.

[32] R.J. Angel, M. Murri, B. Mihailova, M. Alvaro, Stress, strain and Raman shifts, Z. Krist. Cryst. Mater. 234 (2018) 129, https://doi.org/10.1515/zkri-2018-2112.

[33] A.A. Shklyaev, V.A. Volodin, M. Stoffel, H. Rinnert, M. Vergnat, Raman and photoluminescence spectroscopy of SiGe layer evolution on Si(100) induced by dewetting, J. Appl. Phys. 123 (2018), 015304, https://doi.org/10.1063/1.5009720.

[34] J. Wang, Z. Jia, C. Lv, Enhanced Raman scattering in porous silicon grating, Opt. Express 26 (2018) 6507, https://doi.org/10.1364/OE.26.006507.

[35] S. Tamang, K. Kim, H. Choi, Y. Kim, S. Jeong, Synthesis of colloidal InSb nanocrystals via in situ activation of InCl3, Dalton Trans. 44 (2015) 16923, https://doi.org/10.1039/c5dt02181b.

[36] P. Bartlett, D. Cook, C. de Groot, A. Hector, R. Huang, A. Jolleys, G. Kissling, W. Levason, S. Pearce, G. Reid, Non-aqueous electrodeposition of p-block metals and metalloids from halometallate salts, RCS Adv. 3 (2013) 15645, https://doi.org/10.1039/c3ra40739j.

[37] M. Vanaja, G. Annadurai, Coleus aromaticus leaf extract mediated synthesis of silver nanoparticles and its bactericidal activity, Appl. Nanosci. 3 (2013) 217, https://doi.org/10.1007/s13204-012-0121-9.

[38] F. Koohpeima, M. Mokhtari, S. Khalafi, The effect of silver nanoparticles on composite shear bond strength to dentin with different adhesion protocols, J. Appl. Oral. Sci. 25 (2017) 367, https://doi.org/10.1590/1678-7757-2016-0391.

[39] J. Brandon, R. Brizard, W. Pearson, D. Tozer, γ-Brasses with I and P Cells, Acta Cryst. 33 (1977) 529, https://doi.org/10.1107/S0567740877003987.

[40] A. Campbell, R. Wagemann, The silver-indium system: thermal analysis, photomicrography, electron microprobe, and X-ray powder diffraction results, Can. J. Chem. 48 (1970) 1703, https://doi.org/10.1139/v70-281.

[41] P. Wang, J. Kim, C. Lee, Intermetallic Reaction of Indium and Silver in an Electroplating Process, J. Electron. Mater. 38 (2009) 1860, https://doi.org/10.1007/s11664-009-0845-9.

[42] N. Hirashita, Y. Moriyama, S. Takagi, Deformation induced holes in Ge-rich SiGe-on-insulator and ge-on-insulator substrates fabricated by Ge condensation process, Appl. Phys. Express 1 (2008), 101401, https://doi.org/10.1143/APEX.1.101401.